Influence of Arctic sea-ice variability on Pacific trade winds

Charles F. Kennel[a,b,1] and Elena Yulaeva[c]

[a]Scripps Institution of Oceanography, University of California San Diego, La Jolla, CA 92093; [b]Centre for Science and Policy, University of Cambridge, CB2 3BU Cambridge, United Kingdom; and [c]San Diego Supercomputer Center, University of California San Diego, La Jolla, CA 92093

Contributed by Charles F. Kennel, December 3, 2019 (sent for review October 25, 2017; reviewed by Ivana Cvijanovic, Jennifer Francis, and James E. Overland)

A conceptual model connecting seasonal loss of Arctic sea ice to midlatitude extreme weather events is applied to the 21st-century intensification of Central Pacific trade winds, emergence of Central Pacific El Nino events, and weakening of the North Pacific Aleutian Low Circulation. According to the model, Arctic Ocean warming following the summer sea-ice melt drives vertical convection that perturbs the upper troposphere. Static stability calculations show that upward convection occurs in annual 40- to 45-d episodes over the seasonally ice-free areas of the Beaufort-to-Kara Sea arc. The episodes generate planetary waves and higher-frequency wave trains that transport momentum and heat southward in the upper troposphere. Regression of upper tropospheric circulation data on September sea-ice area indicates that convection episodes produce wave-mediated teleconnections between the maximum ice-loss region north of the Siberian Arctic coast and the Intertropical Convergence Zone (ITCZ). These teleconnections generate oppositely directed trade-wind anomalies in the Central and Eastern Pacific during boreal winter. The interaction of upper troposphere waves with the ITCZ air–sea column may also trigger Central Pacific El Nino events. Finally, waves reflected northward from the ITCZ air column and/or generated by triggered El Nino events may be responsible for the late winter weakening of the Aleutian Low Circulation in recent years.

Arctic sea ice | decadal variability | Pacific trade winds | Central Pacific El Nino | Aleutian Low

Forty years ago, Manabe and Stouffer (1) showed that the Arctic surface temperature increases significantly faster than the global mean surface temperature (GMST) in response to increasing greenhouse-gas concentrations. Two feedback mechanisms, from greenhouse warming due to water vapor transported into the Arctic and from increased absorption of sunlight due to seasonal loss of Arctic sea ice and snow cover, are responsible for this "Arctic amplification." The balance of the two mechanisms changed near the end of the 20th century. The change in Arctic climate that started at that time proved due primarily to increase in summer losses of sea ice (2). That change was subsequently related to changes in the duration and pattern of midlatitude extreme weather events (3, 4). Here, we investigate whether the increased loss of summer Arctic sea ice was also related to the changes in trade-wind strength and El Nino behavior observed in the Tropical Pacific.

Recent Change in Arctic and Tropical Pacific Climatology

Two assessments of Arctic climate published 7 y apart illustrated how rapidly Arctic climate dynamics had shifted. The 2004 Arctic Climate Impact Assessment (ACIA) (5) created a 20th-century baseline to which the 21st-century climate could be compared. ACIA's 2011 sequel, the Snow, Water, Ice, and Permafrost Assessment (SWIPA) (6), found that a structural transformation had taken place in the 7 y separating the two assessments. The rate of increase of Arctic mean surface temperature between 2004 and 2011 was the largest on record. Warming had been greater over land before 2004, but between 2004 and 2011, the larger warming rate was over ocean. This was an indication that the sea-ice component of Arctic amplification had strengthened.

Satellite measurements of the earth's radiation budget confirmed that the Arctic's absorption of short-wave solar radiation increased during the period documented by ACIA (7). The summer sea-ice melt uncovers areas of dark ice-free ocean that absorb 93% of the short-wave solar radiation reaching the surface, whereas white ice reflects 50 to 80% back to space. Snowmelt has a comparable effect (8). The Arctic surface heating by solar short-wave radiation increased by 2 W/m^2 between 1979 and 2000; between 2001 and 2011, solar forcing increased by another 4 W/m^2, consistent with the larger decreases in sea-ice area after the turn of the 20th century. When spread over the surface of the earth, the increase in Arctic forcing from 1979 to 2011 was about one-fourth of the increase due to anthropogenic carbon dioxide during the same period. This and other lines of evidence indicated that the large summer losses of sea ice were contributing to changes in Arctic climate (9) judged so fundamental that a 2013 review article (10) was entitled "The Arctic Shifts to a New Normal."

The Arctic and the globe had embarked on diverging surface-temperature trajectories at about the same time. In colloquial terms, global warming decelerated, while Arctic warming accelerated. The period of decelerated GMST increase, which has been called the "hiatus" in global warming (11), provoked conflicted public (12) and policy (13) debates. Scientifically, by 2015, it became clear that the 5th Coupled Modeling Intercomparison Project

Significance

By 20th-century standards, the Central Pacific trade winds that drive the El Nino–Southern Oscillation feedback system to instability have been unusually strong in the 21st century. The annual summer melts of Arctic sea ice are up to twice as large in area as in the 20th century. Arctic sea ice, upper atmospheric circulation, surface wind, and sea-surface temperature data provide evidence that upper troposphere transport processes connect the increased summer losses of Arctic sea ice to the trade-wind and Central Pacific El Nino events characteristic of the present climate state. These results add to the evidence that loss of Arctic sea ice is having a major impact on climatic variability around the world.

Author contributions: C.F.K. and E.Y. designed research; C.F.K. and E.Y. performed research; C.F.K. and E.Y. analyzed data; and C.F.K. wrote the paper.

Reviewers: I.C., Lawrence Livermore National Laboratory; J.F., Rutgers University; and J.E.O., National Oceanic and Atmospheric Administration Pacific Marine Environmental Laboratory.

The authors declare no competing interest.

Data deposition: Derived data that support the findings of this paper and associated codes are available in the GitHub repository at https://github.com/eyulaeva/PNAS-2017-17707.

[1]To whom correspondence may be addressed. Email: ckennel@ucsd.edu.

This article contains supporting information online at https://www.pnas.org/lookup/suppl/doi:10.1073/pnas.1717707117/-/DCSupplemental.

First published January 27, 2020.

(CMIP5) climate model ensemble did not account for the behavior of the GMST, tropical trade winds, and Arctic sea ice during the hiatus. However, subsurface ocean heat content (OHC) did increase at the rate expected from the increase in greenhouse-gas concentrations (14). Anthropogenic forcing had evidently not diminished, but its effects were distributed differently within the climate system. Empirical studies of decadal climate variability provided a candidate explanation. Pacific Ocean sea-surface cooling following the 1998 to 2000 switch in phase of the Interdecadal Pacific Oscillation (IPO) may have offset the previous rate of increase of GMST (15) in a way that the CMIP5 ensemble did not capture (though particular models were more successful).

The El Nino event of 1997 to 1998, the largest in the instrumental record, marked an abrupt change in Tropical Pacific climate. In the year following that event, unusually strong trade winds in the Central Pacific (CP) (16), a long period of La Nina-like cooling of the CP and Eastern Pacific (EP) sea surface (17, 18), and increased ocean heat sequestration in the CP and Western Pacific (19) all began. A 2nd type of El Nino event, the CP El Nino (20–25), found only once in instrumental data before 1990 (26), became the dominant type of El Nino event. Proxy data show that the ratio of CP to EP events was the largest in four centuries (27). CP El Nino events produced long-distance teleconnections (23) that differed from those of the EP El Nino, and an Indian Ocean counterpart to the CP El Nino—the *Ningaloo Nino*—was identified (28).

The first decade of the 21st century, 2000 to 2010, was called a "decade of weather extremes" (29, 30). The severe North American winter of 2009 to 2010 was traced to Arctic air invading the midlatitudes in deep meanders of the jet stream (31). The Moscow heat wave and Pakistani flooding in the summer of the same year were also attributed to a slowly moving meander (32). By 2012, researchers were debating whether the changing pattern of midlatitude extreme weather events and the increased summer losses of Arctic sea ice (3) were related. Though the scientific debate remains vigorous (33–35), the case is strengthening that the larger melts of Arctic sea ice are altering the spatial pattern and intensity of midlatitude extreme weather events (36, 37).

All in all, a change in decadal climatic behavior occurred during the last 2 to 3 y of the 20th century. It required the first decade of the 21st century to confirm the new trends, but the reduced rate of GMST increase, increased summer losses of Arctic sea ice, strengthened CP trade winds, increased frequency of CP El Nino events, cooled sea surface in the equatorial CP and EP, and changed midlatitude extreme weather patterns proved to be components of the new climate configuration. Many of the new features are consistent with a positive-to-negative switch in phase of the IPO, but the magnitude of Arctic sea-ice loss and the strength of the CP trade winds are unprecedented in the instrumental record and unique to the present IPO phase.

Conceptual Model, Methods, and Data

Climate-model ensembles are an objective way to assess the multidecadal impacts of anthropogenic greenhouse-gas emissions on global climate. However, the CMIP 5 ensemble did not account for the reduction in GMST growth rate (38), trade-wind intensification (16), and increased seasonal losses of sea ice after the 1997 to 1998 El Nino (39, 40). Until these shortcomings are diagnosed, questions will remain about how models portray climate variability on the decadal time scale. Using observational data to trace connections between physical processes provides independent information, but it has a cost. Causal ambiguities must be resolved by assuming the time order of those processes. This is done here by postulating an extension of the conceptual model proposed to explain the influence of sea-ice variability on midlatitude extreme weather:

1) Vertical convection is generated in episodes of about 1-mo duration over the ice-free areas in the Pacific-facing sector of the Arctic Ocean in early boreal fall (*Initiation, Duration, and Spatial Extent of Convection Episodes*);
2) Vertical convection episodes stimulate a planetary wave and a southward-propagating higher-frequency wave train in the upper troposphere that interact with the Indo-Pacific Intertropical Convergence Zone (ITCZ) in December (*P2 Arctic ITCZ-Teleconnections*, *Difference between P1 and P2 Teleconnections*, and *Southward Advance of P2 Teleconnections*);
3) The interaction of the wave and wave train with the ITCZ air column creates conditions favorable to triggering CP El Nino events (*Westerly Wind Bursts and the CP El Nino*);
4) A reflected northward propagating wave and wave train is created in the interaction of the Arctic-origin waves with the ITCZ air column (*Westerly Wind Bursts and the CP El Nino* and *Arctic Sea Ice and the Aleutian Low Circulation*);
5) The Aleutian Low Circulation responds to the passage of the reflected waves over the North Pacific in February (*Arctic Sea Ice and the Aleutian Low Circulation*);
6) The cumulative impact of repeated large annual losses of September Sea ice shapes the climatology of the Northern Pacific after 1999 (*Recent Change in Arctic and Tropical Pacific Climatology*).

The sequence of events 1 to 5 repeats annually, but the intensity and spatial structure of the annual episodes of convection vary due to contingent factors like clouds, storms, and water vapor content in the Arctic atmosphere (41, 42). Snow cover, surface roughness, and melt-water ponding affect sea-ice albedo and thus its melt rate, influencing when and where convection episodes start and stop. The amplitude of a convection episode may be thought of as a product of intensity, area, and duration; despite the seasonal regularity of solar insolation, the timing and amplitude of Arctic convection episodes vary from year to year.

This paper investigates how tropical Pacific climate adjusts to changes in amplitude of Arctic convection episodes. Components of the climate system that respond to convection episodes may be identified by regression on September sea-ice area (SSIA). The late 20th century was a "high ice" period (smaller summer sea-ice loss) and the 21st century a "low-ice" period (larger loss); the data from the 2 periods are binned separately to highlight the change in relationship between Arctic sea ice and tropical climate noted in *Recent Change in Arctic and Tropical Pacific Climatology*. Many models of the impacts of Arctic sea-ice variability on extra-Arctic climate have not been energy conserving. By comparing the results of "low-ice" and "high-ice" energy-conserving climate models, Cvijanovic et al. (43) found that the Aleutian Low Circulation in the North Pacific could be influenced by Arctic Sea-ice loss via a 2-step teleconnection: Arctic to Tropical Pacific and Tropical Pacific to North Pacific. These results add to the case that the recent changes in Arctic sea ice are having important effects on midlatitude climate.

For this paper, however, the 2-step teleconnection is the important idea; Matsumura and Kosaka (44) propose a related picture. The view emerging from Cvijanovic et al. is consistent with steps 1, 2, 4, and 5 in the sequence above. Their results lend confidence to the use here of that sequence of steps to interpret statistical analyses that viewed singly are ambiguous. Viewed together, the empirical analyses presented here support their picture, identify climatic processes that respond to SSIA variability, and characterize the differences between the 2 high-ice decades before the turn of the 20th century and the 2 low-ice decades that followed.

The properties and limitations of the public-domain data used here have been extensively documented. Atmospheric variables and sea-surface temperature (SST) were derived from the National Centers for Environmental Prediction (NCEP)/National Center for Atmospheric Research (NCAR) reanalysis monthly means (45, 46) or from the daily European Centre for Medium-Range Weather Forecasts interim Reanalysis (ERA-Interim) (47).

The ERA-Interim product has proven superior for high-latitude studies (48, 49). Arctic Sea Ice area was calculated by using the National Oceanic and Atmospheric Administration (NOAA)/National Snow and Ice Data Center (NSIDC) Climate Data Record of Passive Microwave Sea Ice Concentration, Version 3 (50, 51). Sea-surface height (SSH) relative to the geoid was obtained from NCEP Global Ocean Data Assimilation System (GODAS) Reanalysis data (52) provided by the NOAA/OAR (Oceanic and Atmospheric Research) Earth System Research Laboratory's Physical Sciences Division, Boulder, CO, from their website at https://www.esrl.noaa.gov/psd/. Derived data that support the findings of this paper and associated codes are available in the GitHub repository at https://github.com/eyulaeva/PNAS-2017-17707.

The 1997 to 1998 Transition in Equatorial Pacific Climate

The Hovmuller diagrams (53) in Fig. 1 display the longitude and time dependences of the monthly anomalies relative to 1980 to 1998 climatology of SSH, SST, sea-level pressure (SLP), and 10-m zonal wind velocity (SSU) averaged over ±7.5° latitude. SSTs exceeding 26 °C to 28 °C are required to drive the deep atmospheric convection generated by storms over tropical oceans (54, 55). The superposed black lines convey the time-dependence of the longitude of the 29 °C isotherm, which locates the longitude where the measured SST averaged over a ±7.5° latitude band equaled 29 °C. A sharp gradient in sea-surface salinity (SSS) (the "barrier") has been found near the 29 °C isotherm and to move east and west with it (56, 57). The salinity barrier effectively defines the eastern boundary of the Western Pacific Warm Pool (WPWP), and its association with the 29 °C isotherm provides a way to track its motions by using SST data, whose time series is much longer than that of SSS.

The SSH, SLP, SSU, and SST time series changed character after the 1997 to 1998 El Nino event, which is identified by the positive SST anomaly in Fig. 1, *Lower Left*. The trade winds (SSU) strengthened in the year after the event. Strong easterly anomalies (blue) appeared in the CP (165°W to 150°E) in 1999 and in the 2 following years; they were again strong between 2007 and 2014 and after the 2015 El Nino event. They were the strongest in a century-long data record at these times (16). SSH was generally lower and SLP generally higher in the EP after the 1997 to 1998 event. Transient El Nino events characterize the change in SST behavior in the CP, but more persistent change is clear west of the 29 °C isotherm: SST in the WPWP increased after the 1997 to 1998 El Nino event and remained elevated.

Easterly trade-wind anomalies in the CP were accompanied by westerly anomalies in the EP (90°W to 150°W) after 1999. We call the combination of opposite-sign anomalies the Trade-Wind Dipole Anomaly. The 29 °C isotherm is the western boundary of the trade-wind dipole anomaly. Inspection of Fig. 1 reveals that when the 29 °C isotherm was in the Western (Central) Pacific, the dipole anomaly was strong (weak), and westerly winds in the WPWP were weak (strong).

We define a trade-wind dipole anomaly index by averaging the NCAR/NCEP 10-m zonal wind velocity over areas N4 and N3, spanning the equatorial CP and EP, respectively, and taking the difference. N4 and N3 have the same longitudinal extents as the Nino4 (150°W to 160°E) and Nino3 (90°W to 150°W) regions (58) used in El Nino–Southern Oscillation (ENSO) forecasting, but their latitudinal extents are increased from ±5° to ±7.5° to include the Northern Hemisphere latitude where the ITCZ is typically found in boreal winter. The difference of the N3 and N4 averaged 10-m wind velocities, U3 − U4, is the trade-wind dipole index.* The Trade-Wind Dipole Anomaly and the Southern Oscillation Indices are shown to be comparable indicators of El Nino event likelihood in *SI Appendix*, section S2.

To characterize the consequences of the transition in decadal climate documented here, data will be binned into sets of approximately equal duration preceding and following the transition. The SSIA time series does not provide an unambiguous choice of transition year; however, the 1997 to 1998 El Nino event did mark a definite shift in Equatorial Pacific climatic behavior. We chose 1998 to be the transition year and defined P1 to be the period from 1980 and 1998 and P2 to be the period from 1999 to 2015. P2 to P1 epoch difference maps of the four variables in Fig. 1 are presented in *SI Appendix*, section S1.

P1 and P2 El Nino Events

Eastward displacement of the 29 °C isotherm to the CP sets the stage for EP and CP El Nino events (59–61), named according to longitude of origination. The signature of the EP El Nino is a positive SST anomaly that originates in the EP and spreads westward, whereas that of the CP El Nino is a positive SST anomaly that originates in the CP (23) and spreads eastward. The positive SST anomalies (red) in Fig. 1, *Lower Left* document El Nino events that occurred during P1 and P2. There were three EP (1982, 1987, and 1998) and three CP (1992 to 1995) events in P1 and eight CP events of varying strength, one incomplete EP event (2014), and one completed EP event (2015) in P2.

Both kinds of El Nino event in Fig. 1 occurred at times of maximum eastward displacement of the 29 °C isotherm. The maximum displacement longitude was for all practical purposes the starting longitude for CP El Nino events; the 29 °C isotherm retreated westward after the CP events started. By contrast, maximum eastward displacement occurred before one and during the three other EP events between 1979 and 2017. In all four EP cases, the 29 °C isotherm returned westward after the events.

Correlation of September Sea-Ice Concentration with December Trade-Wind Dipole Anomaly Index

According to the conceptual model in *Conceptual Model, Methods, and Data*, upper tropospheric waves launched during convection episodes take 1 to 2 mo to propagate from the Arctic and interact with the trade winds in the vicinity of the ITCZ. If so, one might expect to find delayed correlations between sea-ice area in September and trade winds in December. Let P1 September and P2 September denote the sets of monthly average data for all of the months of September in the P1 and P2 time intervals, respectively, and adopt analogous terminology for other months. Fig. 2, *Upper* (Fig. 2, *Lower*) maps the correlation between P1 (P2) September Sea-Ice Concentration (SSIC) data and P1 (P2) December trade-wind dipole index data. Negative correlation (blue) implies that an SSIC decrease at that location in September contributes to an increase in trade-wind dipole index in December, and vice versa for positive correlation (red).

The sea-ice edge in the Pacific-facing sector of the Arctic (90°W to 180° to 90°E) retreats northward from the coastlines during the summer ice melt and advances southward toward the coastlines during the fall refreeze. In P2 data, the strongest correlations are concentrated in the region of retreat and advance: a thin blue band of high negative correlation ($r = -0.8$) north of the coastline from the Beaufort Sea to the Laptev Sea. SSIC was less than 15% in the region devoid of data between the high correlation band and the coasts. This is a region of nearly complete ice melt (62), where solar heating of the ocean is intense and upward atmospheric convection is likely. The band of large negative correlation poleward of the no-data region is the ice edge. Since the correlation is negative around the Beaufort–Laptev sector, poleward retreat (equatorward advance) of the ice edge would increase (decrease) the trade-wind dipole index.

The spatial pattern of September–December correlations was different in P1 and P2 data. In P1 data, there were no zero-data regions (that is, sea ice rarely left the coasts) and no regions

*By convention, U positive (negative) corresponds to westerly (easterly) wind direction. Positive (negative) U3 to U4 corresponds to La Nina (El Nino) conditions.

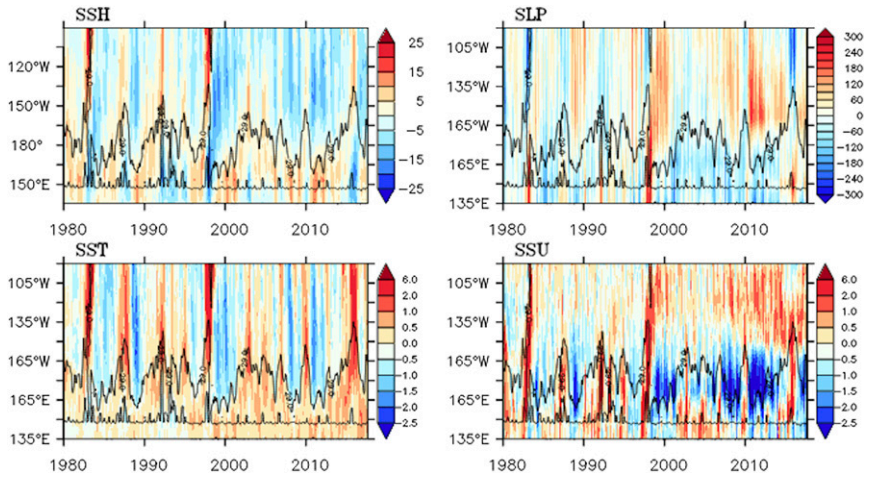

Fig. 1. ENSO-related diagnostics, 1980 to 2017. Time-longitude Hovmuller diagrams of monthly anomalies (relative to P1 = 1980 to 1998 monthly climatology) of SSH (cm) (*Upper Left*), SLP (Pa) (*Upper Right*), SST (°C) (*Lower Left*), and the zonal component of the 10-m wind velocity (SSU, m/s) (*Lower Right*) are shown. SST, SSU, and SLP were derived by averaging the corresponding NCAR/NCEP Reanalysis data over the ±7.5° latitude belt and plotted as a function of longitude in the equatorial Pacific Sector from 135° E to 90° W (vertical axis) with time extending from 1980 to 2017 (horizontal axis). SSH was derived by averaging SSH relative to the geoid from the NCEP GODAS Reanalysis over the same latitude belt. The black line traces the time history of the longitude of the 29 °C isotherm.

where the correlations were as large as in P2 data. In P1 data, the regions bounding the North American and Siberian coasts had mixed positive and negative correlation, positive ($r = +0.6$) near the Beaufort Sea coast and mostly negative ($r = -0.4$) near the East Siberian and Laptev Sea coasts. If ice-edge retreat or advance in a given year were uniform around the Beaufort–Laptev sector, one would expect the change in the P1 trade-wind dipole index to be small, since the contributions from the positive and negative correlation regions would offset one another.

In summary, monthly December trade-wind dipole indices correlate with SSIC spatial variability in both P1 and P2 data. The P2 correlation is particularly strong ($r = -0.8$) in an annular band extending from the Beaufort Sea to the Laptev Sea that can be identified with the sea-ice edge. The strength and location of the high correlation band suggests that ice-edge movement to the north (south) in September will correlate with increase (decrease) in trade-wind dipole index in December. The following sections assess the links in the chain of processes that connect Arctic sea ice to trade winds. That chain starts in the region of warmed ocean, where sea ice retreats and advances and vertical convection is initiated in early fall.

Initiation, Duration, and Spatial Extent of Convection Episodes

Fig. 3 displays maps of the static stability (63) of the atmosphere 80 m above the Arctic region selected from a sequence of 11-d averages computed from ERA-interim data center displaced by 5 d from August 1 to December 1. ERA-5 data were used to map convectively available potential energy in the same format (not shown). The two sets of results both identify a region of instability with the seasonally ice-free area of open ocean in the Pacific-facing sector (90°W to 180° to 90°E). The 1949 to 2017 time history of Pacific Sector open-water area is presented in *SI Appendix*, section S3.

The timings and spatial extents of the unstable regions in P1 and P2 data differed. In both periods, the atmosphere at 80-m altitude was stable (red) in August, unstable (blue) in parts of September and October, and stable in November and December. The left- and right-hand columns of Fig. 3 *Upper Left*, *Lower Left*, *Upper Right*, and *Lower Right* show the static stability maps when instability first (*Left*) and last (*Right*) appeared in P1 (*Upper*) and P2 (*Lower*). Instability appeared first and disappeared last near the New Siberian Islands, straddling the Laptev and East Siberian Seas in both P1 and P2 data. Instability started 10 d earlier in P1 than in P2 and ended 15 d later in P2. P1's unstable period lasted 40 d, and P2's 45 d. The regions of instability were located north of the North American and Siberian coastlines but differed in poleward extent in P1 and P2 data. Fig. 3, *Upper Center* and *Lower Center* show the 11-d intervals when the unstable regions achieved the largest area. The solid lines denote the P1 or P2 average SSIA sea-ice edge at the time of maximum sea-ice loss. The unstable region extended from the coasts to the sea-ice edge in both P1 and P2 data.

Additional assumptions and calculations would be necessary to convert Pacific-facing sector ice-free area to convection episode amplitude. There is, however, a practical approach to testing hypothesis 2 of *Conceptual Model, Methods, and Data*: regress on SSIA, which is routinely measured. SSIA is not a perfect proxy for episode amplitude, because contingent factors like cloudiness (64) and storms (65) affect convection thresholds and rates. Nonetheless, regression on SSIA does identify extra-Arctic climatic processes that respond to changes in the annual minima of Arctic sea-ice area.[†]

P2 Arctic-ITCZ Teleconnections

To proceed further, it is helpful to describe hypothesis 2 of *Conceptual Model, Methods, and Data* with more specificity. Convection episodes inject heat and moisture into the upper troposphere near the end of every sea-ice melt season. The upward baroclinic flow is neither spatially uniform nor steady and creates variability of the general circulation at high altitude that has high- and low-frequency content. A convection episode lasts around a month, so variability should be created on the monthly time scale—for example, by generating low-frequency planetary waves that modulate the midlatitude jet stream (66, 67). The input into the upper troposphere is the cumulative result of transient convection events that take a few days to rise and fall. Their space–time variability generates monthlong trains of higher-frequency waves with periods of 2.5 to 6 d (66). In such

[†]A static instability region develops south of the ice edge in the Atlantic-facing sector (90°E to 0° to 90°W) in September and persists until at least December in P1 and P2 data. This unstable area is probably not due to ocean warming following reduction in Arctic sea-ice area since the calculations show instability in regions south of the ice edge in November and December where sea ice is found only in iceberg form.

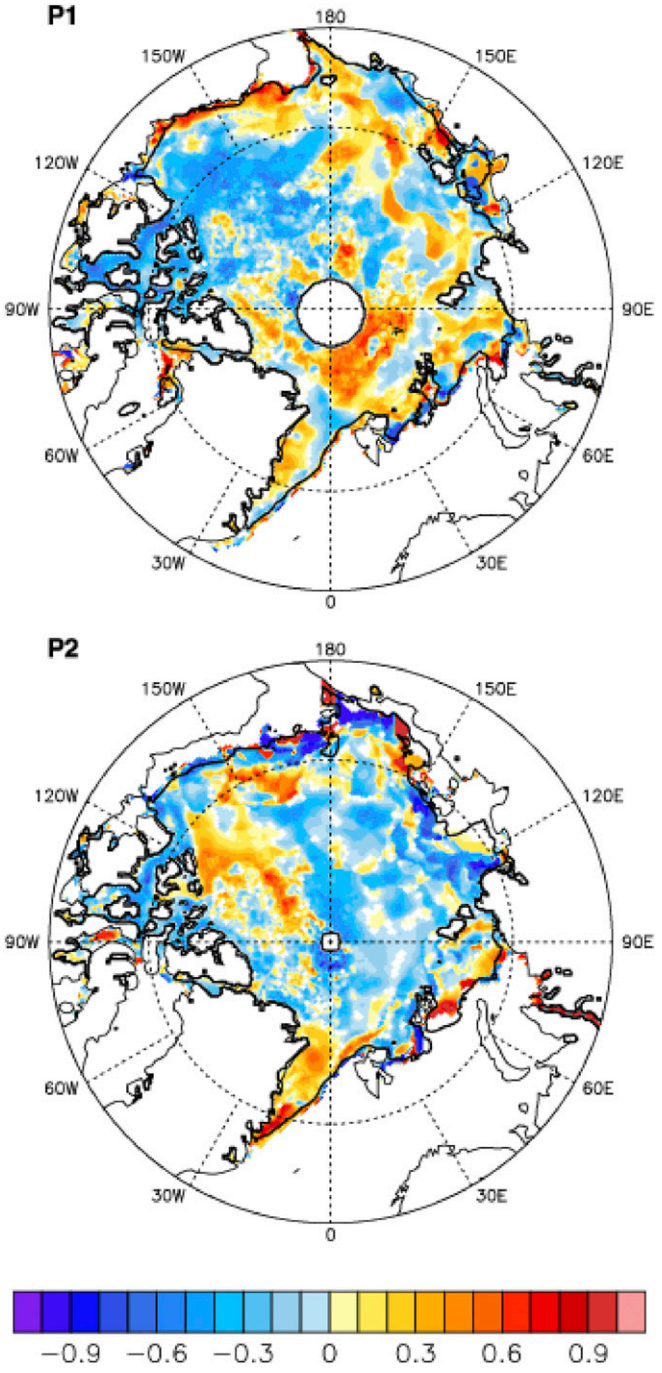

Fig. 2. Lagged correlation between the September sea-ice concentration and the December trade-wind dipole index. Maps show the correlation between the December trade-wind dipole index and sea-ice concentration (SIC) during the preceding September for P1 (*Upper*) and P2 (*Lower*). SIC data were taken from the NOAA/NSIDC passive microwave data record. The southernmost latitude is 67° North. Thick line denotes 15% SIC contour.

cases, the planetary waves would provide most of the momentum transport (68), but the higher-frequency wave trains act to reduce the Equator-to-pole temperature gradient. Wave transport continues in the upper troposphere, even after sea-ice regrowth frustrates convection over the Arctic Ocean. Midlatitude weather is affected 1 to 2 mo later (33, 69–71), though exactly how has been controversial (72).

P2 Arctic ITCZ-Teleconnections, *Difference between P1 and P2 Teleconnections*, and *Southward Advance of P2 Teleconnections* are concerned with the planetary wave/wave-train interaction with the ITCZ air column. Except in the jet streams and ITCZ air column, the circulation in the upper troposphere is quasi-geostrophic (73); that is, dissipation- and divergence-free on constant pressure surfaces; the wind velocity is derivable from a scalar function—the stream function—on those surfaces. Stream function contours characterize the teleconnections established by the combined actions of the low-frequency planetary wave and the higher-frequency wave train.

Figs. 4–6 present the results of regressions of the stream function on the SSIA. All three figures derive from NCAR/NCEP reanalysis data and have the same format. The 300-mb pressure surface was chosen as representative of upper troposphere conditions; calculations not shown exhibit qualitatively consistent behavior for the 100- to 500-mb pressure surfaces. Monthly regression results for 300 mb are presented as anomalies relative to P1 climatology for both P1 and P2 data; the P1 SD in SSIA is the measure of sea-ice variability for both P1 and P2. All three figures show the response to a decrease in P2 SSIA of one 1 P1 SD.

The P2 December stream function response map (Fig. 4, *Upper*) has three closed-contour cells that extend across the Pacific to the tropics. The boxes locate the areas N4 and N3 used to calculate the trade-wind dipole index (*P1 and P2 El Nino Events*). The northernmost (and strongest) cell originates over the East Siberian Sea–Barents Sea coastal arc that contains the region of observed maximum sea-ice retreat and delay of fall refreeze (74). Fig. 3 indicates that convective instability starts and ends in this region. This cell approaches the northern boundary of N3, which is near the typical latitude of the ITCZ in

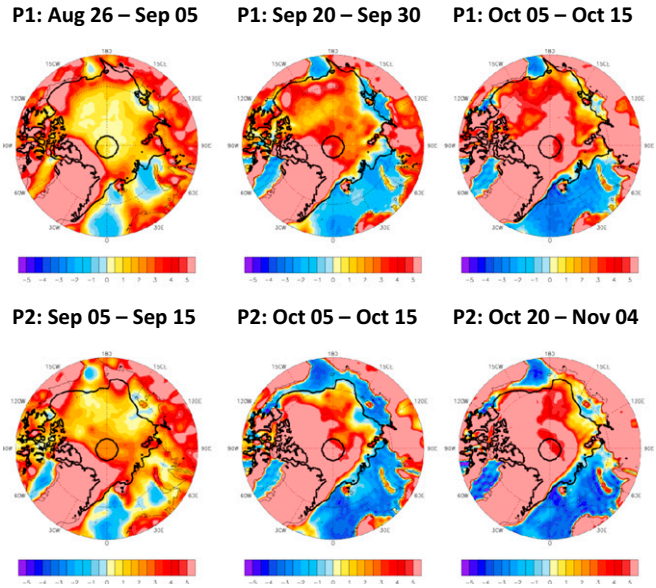

Fig. 3. Time evolution of convective instability regions. ERA-interim data were used to map atmospheric static stability at 80-m altitude above the Arctic Ocean for P1 and P2. For each period, a series of 23 11-d averages with 5-d moving centers running from August 1 to December 1 was created. *Upper* displays P1 maps for August (Aug) 26 to September (Sep) 5 (*Left*), September 20 to 30 (*Center*), and October (Oct) 5 to 15 (*Right*). *Lower* displays P2 maps for September 5 to 15 (*Left*), October 5 to 15 (*Center*), and October 20 to November (Nov) 4 (*Right*). The black lines in each map denote the P1 or P2 average September sea-ice extent. The polar plot ranges are 90° to 67° North latitude, and the units are degrees Kelvin per kilometer. Blue denotes instability.

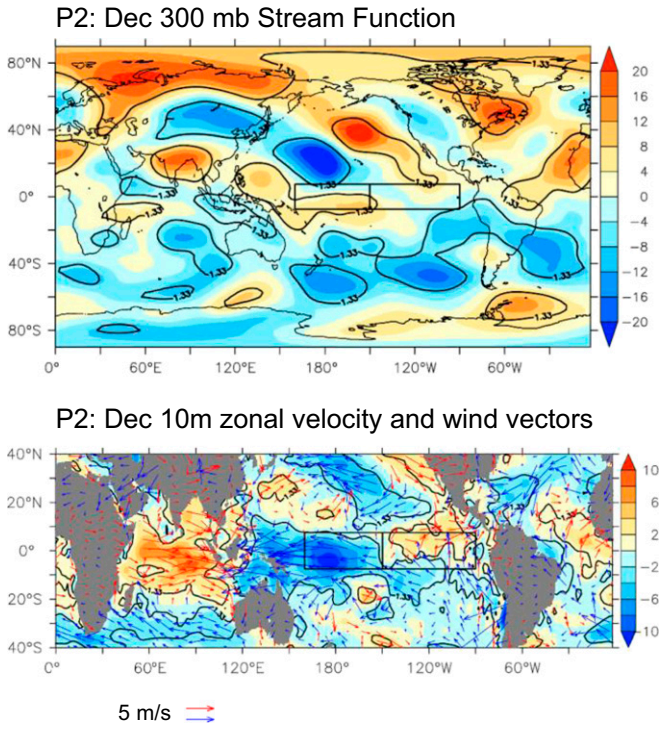

Fig. 4. Three-cell Arctic-Pacific telecommunication pattern. *Upper* shows a regression map of the 300-mb stream function anomalies ($m^2/s \times 10^{-6}$) in P2 December on the time series of the preceding P2 September Arctic sea-ice area anomalies. All anomalies are with respect to P1 climatology, and the regressions are scaled to a (−1) SD reduction of the P1 Arctic SSIA. *Lower* superposes regressed atmospheric 10-m wind-vector anomalies (blue easterly and red westerly) on the regressed 10-m zonal velocity anomaly (m/s) (color contours). The boxes locate the regions N3 and N4 used to define the trade-wind dipole anomaly. The arrow lengths at the bottom denote wind velocity of 5 m/s, with easterly in blue and westerly in red. The solid contours enclose areas where regression coefficients differ from zero with more than 90% confidence according to Student's *t* test.

the EP, about 7.5°N (75). The second, more southerly cell approaches the northern boundary of N4 in the CP, again, close to the expected latitude of the ITCZ. The third cell connects South Asia to the southern boundary of N4 in the Western Pacific.

The three cells have alternating signs: Their stream functions are positive–negative–positive north to south. Since flow circulates counterclockwise (cyclonically) around a stream function maximum and clockwise (anticyclonically) around a minimum in the Northern Hemisphere, conservation of angular momentum implies that anomalies with these circulation senses would be communicated to the surface winds below. The regressed 10-m wind anomalies in N3 and N4 are consistent with the signs of the 300-mb stream-function anomalies at the northern boundaries of N3 and N4. Fig. 4, *Lower* shows 10-m wind vectors superposed on color contours of the zonal wind-velocity anomalies calculated for the same regression parameters as in Fig. 4, *Upper*. The wind-anomaly vectors are easterly (blue) in N4 and mostly westerly (red) in N3, indicating that the trade-wind dipole anomaly is created when the anomalous upper tropospheric circulation in the two northernmost cells interacts with the ITCZ air column.

Difference between P1 and P2 Teleconnections

The P1 and P2 atmospheres had different structures (76) and therefore different teleconnection pathways. Fig. 5 compares the P1 (*Left*) and P2 (*Right*) regressions on SSIA of the December 300-mb stream function (*Top*), 10-m zonal velocity (*Middle*), and SST (*Bottom*). The P1 analog of the P2 northern teleconnection cell connects to the region of maximum sea-ice loss as in P2, but turns eastward at midlatitudes and does not reach the ITCZ. This teleconnection pattern signifies a remote sea-ice influence on midlatitude North American circulation, but not on tropical Pacific circulation. The P1 stream function has the same sign over the northern boundaries of N3 and N4, implying there should be no trade-wind dipole anomaly. Accordingly, the regressed 10-m zonal wind velocities in Fig. 5, *Left Middle* have largely the same sign in N3 and N4.

The P1 and P2 regression responses of December SST are shown in Fig. 5, *Bottom*. In P1 data, an SSIA decrease generated small SST responses everywhere except in the Atlantic Gulf Stream near the North American East Coast. In P2 data, an SSIA decrease produced cooling responses in N4 and N3 and warming responses in both the WPWP and the midlatitude North Pacific. Note that an SSIA decrease of the same magnitude (−1 P1 SD) drove both the P1 and P2 regressions, yet there were significant trade-wind and temperature anomalies only in P2 data. This is an indication that the teleconnections between the Arctic and the Tropics were stronger in P2 than in P1.

Southward Advance of P2 Teleconnections

According to *Initiation, Duration, and Spatial Extent of Convection Episodes and P2 Arctic-ITCZ Teleconnections*, convection episodes generate planetary waves with periods of about a month and wave trains of about a month's duration that take several months to propagate from the Arctic to the Tropical Pacific. If so, the September-to-December sequence of monthly stream-function regression responses should provide low-resolution snapshots of the combined impacts of planetary wave modification of the jet streams and the southward advance of the wave trains.

The P2 300-mb stream-function regression responses mapped in Fig. 6 show an orderly series of changes from September to December. In P2 September, the stream-function cells over the Northern Pacific are zonally aligned; there is no streamline connectivity between the Arctic and lower latitudes. The P2 October stream-function anomaly is not organized into southward-extending structures; except for a small region east of Japan, no streamline connects the Arctic with the Pacific. In P2 November, the three cells identified in Fig. 4 are organized, and there is streamline connectivity between the Arctic and the Northern Pacific. The northern positive cell extends along the North American coast and turns eastward at midlatitudes, while the negative cell lies to its south. The negative cell does not approach the ITCZ, and the stream functions over N3 and N4 have the same sign, implying no trade-wind dipole anomaly. By P2 December, the P2 November northern cell arrives at the ITCZ in N3, its southern neighbor approaches it over N4, and the trade-wind dipole anomaly appears in 10-m wind data.

In summary, P2 September has no 300-mb stream-function structures that connect the Arctic to the Tropical Pacific; P2 December has structures that do link the Arctic to the ITCZ; and P2 October and P2 November are intermediate cases—a sequence consistent with wave-train advance from the Arctic to the Tropical Pacific.

Westerly Wind Bursts and the CP El Nino

According to Fig. 1, eastward displacement of the 29 °C isotherm to the CP sets the stage for both EP and CP El Nino events. Once the stage is set, westerly wind bursts (WWBs) (77–80) trigger them. WWBs are transient wind anomalies of 5- to 20-d duration that temporarily reverse or reduce the velocity of the easterly trade winds; while not every WWB triggers an El Nino event, WWBs were associated with every EP and CP El Nino event between 1971 and 2010 (81).

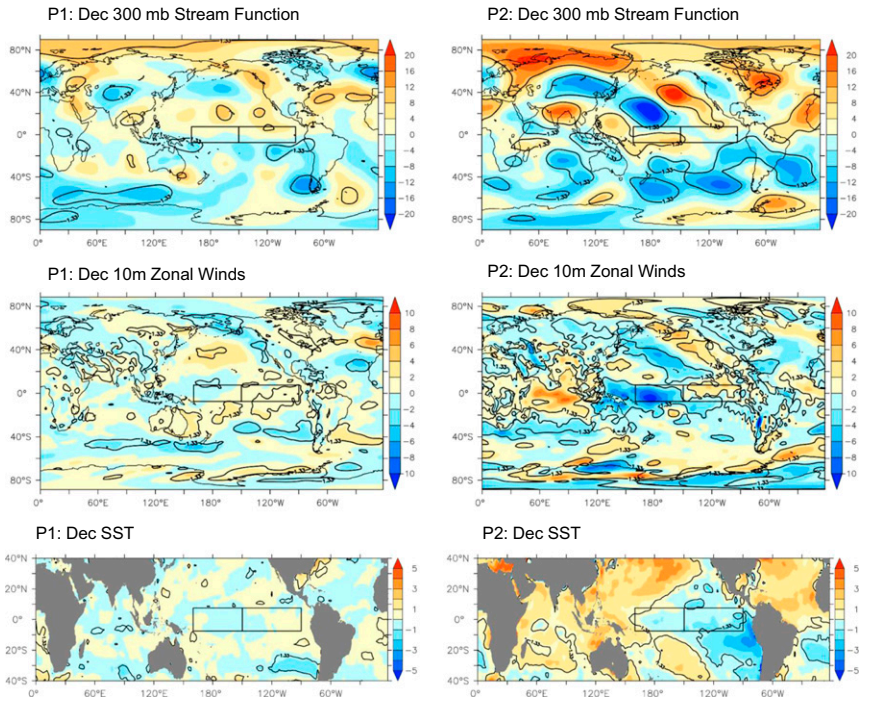

Fig. 5. Regression coefficients of P1 and P2 variables against SSIA. *Top* compares the December (Dec) 300-mb stream-function structures generated by regression on seasonal sea-ice area in P1 (*Left*) and P2 (*Right*). *Middle* shows the regressed zonal component of the 10-m wind velocity, in units of m/s, for P1 (*Left*) and P2 (*Right*). *Bottom* shows the regressed SST (°C) for P1 (*Left*) and P2 (*Right*). The data source, formatting, regression parameters, and contour lines are the same as for Fig. 4.

Fig. 1 indicates that CP El Ninos are triggered near a point of maximum eastward displacement of the 29 °C isotherm that effectively locates the eastern boundary of the WPWP. The transition layer between Warm Pool and CP water is characterized by strong zonal gradients in SST, SSH, and SSS; the CP El Nino is associated with relaxation of those gradients (82). By reducing trade-wind stress on the ocean surface, a WWB over the transition layer releases a shallow eddy-mixed layer of higher-SSH, higher-SST, lower-salinity, lower-density water eastward under gravity; after triggering, WPWP water advects over the lower-SSH, lower-SST, higher-SSS, higher-density CP water (83) to the east of the transition layer. There is little delay between the WWB trigger and the appearance of the positive SST anomaly that moves eastward from the point of triggering.

WWB triggering occurs especially in the months that wave trains generated by Arctic convection episodes interact with the ITCZ air column, since maximum CP El Nino occurrence is in December and January (23). This temporal coincidence motivates two questions. First, are WWBs produced during that interaction? Second, since a larger SSH gradient makes it more

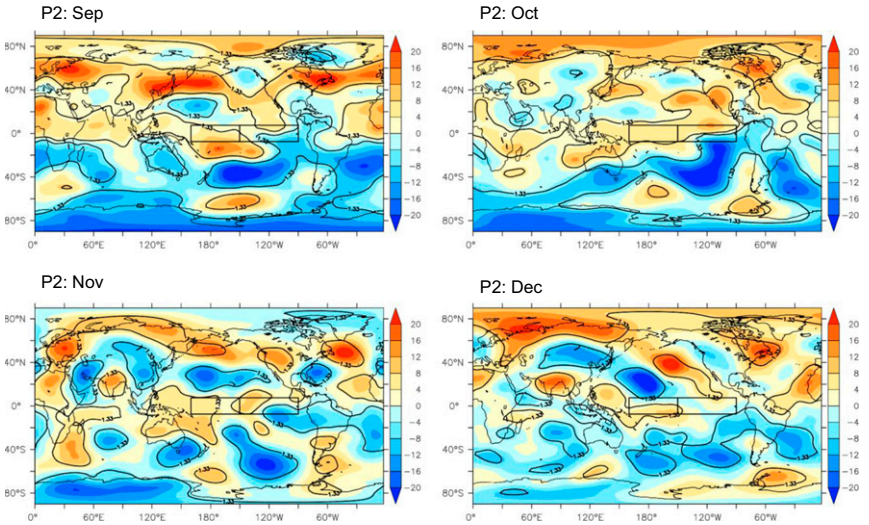

Fig. 6. Monthly evolution of upper troposphere teleconnections. Shown are regression maps ($m^2/s \times 10^{-6}$) for September (Sep; *Upper Left*), October (Oct; *Upper Right*), November (Nov; *Lower Left*), and December (Dec; *Lower Right*) of the 300-mb stream function on the time series of the preceding September Arctic sea-ice area. Regression conditions, formats, and contour-line meaning are the same as in Fig. 4, *Upper*.

likely that a WWB of a given amplitude will trigger a CP El Nino event, does the wave-train interaction with the ITCZ air column increase the SSH gradient in the transition layer?

The 1-mo time resolution of SSIA regression methods cannot diagnose the wave-train interaction with the ITCZ air column, but it is possible to infer certain properties of the interaction using reasoning based upon earlier results in this paper. The area of the Pacific-facing sector of the Arctic Ocean that is unstable to atmospheric convection increases from zero, maximizes, and returns to zero over a 40- to 45-d period (*Initiation, Duration, and Spatial Extent of Convection Episodes*). An Arctic convection episode should therefore comprise a roughly 20-d period of strengthening convection, followed by a 20-d period of weakening convection. The wave trains traveling southward from the Arctic should also strengthen and weaken over comparable periods. During wave-train interaction with the ITCZ air column, the easterly wind speed in the CP should increase, maximize, and decrease (*Correlation of September Sea Ice Concentration with December Trade-Wind Dipole Anomaly Index*), and the decreasing phase could be interpreted as a WWB.

Regression of SSH on SSIA provides indirect evidence about the modification of the SSH gradient by the wave-train interaction with the ITCZ air column. Fig. 7 maps color contours of SST (*Left*) and SSH (*Right*) regressed to −1 P1 SD reduction in SSIA for P2 November (*Top*), P2 January (*Middle*), and P2 February (*Bottom*). The boxes locate the areas N3 and N4 that define the trade-wind dipole anomaly index (*P1 and P2 El Nino Events*). Samples of regressed 10-m wind vectors are mapped on the SST and SSH color contours. The SSH gradient may be visually estimated from the spacing of the SSH contours.

In the model in *Conceptual Model, Methods, and Data*, a wave train of about a month's duration approaches the ITCZ in November (Fig. 6), arrives at the ITCZ in December (Figs. 4 and 6), completes its interaction with the ITCZ air column in January (Fig. 7), and launches a reflected wave train that arrives over the Aleutian Low Circulation in February (Fig. 8). Since P1 wave trains do not reach the ITCZ (Fig. 5), the P1 SSH, SST, and wind regressions show little change between P1 November, P1 January, and P2 February and are not shown. The SSH results for P2 do show significant change. For P2 November, Fig. 7 shows a mild SSH gradient at the western boundary of N4, where CP El Ninos are triggered (Fig. 1). A positive SSH anomaly appears in the Eastern Indian Ocean and in the WPWP in P2 January; the SSH gradient near the western boundary of N4 is strongest in this month. In P2 February, the SSH anomaly in the Eastern Indian and Western Pacific Oceans is smaller than in P2 January, and the SSH gradient near the western boundary of N4 is smaller than in P2 January.

Fig. 7 also contains SSH evidence that processes within the ITCZ respond to sea-ice variability in P2. There is a thin band of negative SSH regression response near the expected position of the ITCZ at the northern edge of N3 in P2 November, P2 January, and P2 February. Regression also detects a parallel structure south of the Equator in N3 in P2 January and P2 February, months that precipitation observations find that a double ITCZ occurs (84). This pair of negative SSH anomalies encloses a negative SST anomaly localized to the geographic equator in these months. Further evidence would be required to confirm that a double ITCZ is a delayed response to reduction in SSIA.

In summary, in P2 data, reduction in SSIA regresses to SSH zonal gradients in the WPWP transition layer favorable to advective instability in the months when convection episode-created wave trains interact with the ITCZ air column. A reduction in trade-wind speed in the diminishing phase of the wave-train interaction would appear as a WWB lasting around 20 d. Fig. 1 indicates that that summer Arctic sea-ice loss does not couple to CP events in years when the 29 °C isotherm is in the far Western Pacific. We do not argue that all WWBs and/or

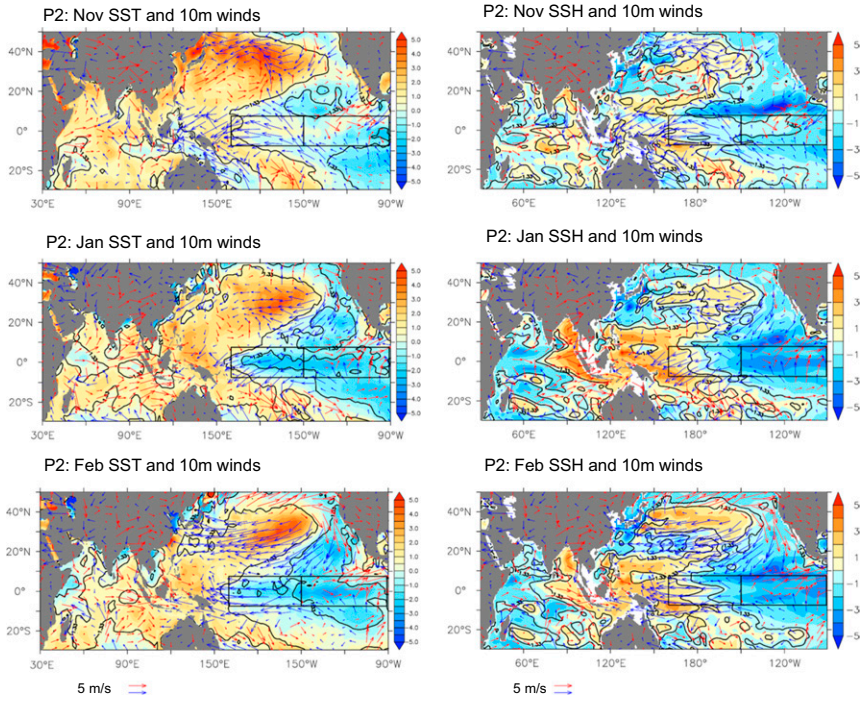

Fig. 7. North Pacific P2 SST, SSH, and 10-m wind regressions. Shown are November (Nov) SST (*Top Left*), November SSH (*Top Right*), January (Jan) SST (*Middle Left*), January SSH (*Middle Right*), February SST (*Bottom Left*), and February (Feb) SSH (*Bottom Right*). The SSH color scale ranges from −5 to 5 dm; the SST color ranges from −5 to 5 °C. The arrow lengths at the bottom of each panel denote wind velocity of 5 m/s, with easterly in blue and westerly in red. The 10-m winds and SST were drawn from NCEP/NCAR and SSH from GODAS data. Regression parameters, N3 and N4 boxes, and contour-line meaning are the same as in Fig. 4.

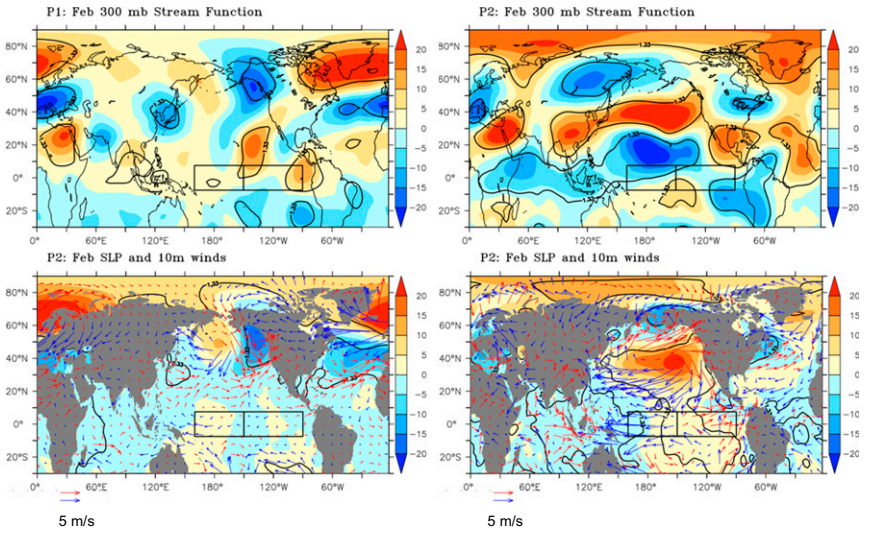

Fig. 8. Northern Pacific teleconnections for the month of February (Feb). *Upper* contours the regressed 300-mb stream function in P1 (*Left*) and P2 (*Right*). The regression conditions, boxes, and contour-line meanings are the same as in Figs. 4–6. *Lower* shows selected 10-m wind vectors superposed on SLP. NCEP/NCAR data were used. The arrow lengths at the bottom denote wind velocity of 5 m/s, with easterly in blue and westerly in red.

CP El Nino events require an Arctic-origin trigger. We do argue that summer sea-ice loss led to SSH gradients more favorable to advection instability in P2 and less favorable in P1 (when summer sea losses were smaller and CP events were not observed as frequently); that SSH gradients favorable to advective instability are generated under regression near where CP events originate; that the switch each fall from sea-ice retreat to advance provides for a westerly wind anomaly on the 20-d time scale in winter; and that those CP events that are Arctic sea-ice-related should be initiated in December and January.

Arctic Sea Ice and the Aleutian Low Circulation

The Aleutian Low Circulation is the dominating feature of winter North Pacific climate, organizing storm systems and the jet stream (85). The Aleutian Low Circulation changed character in the late 1990s when CP El Ninos began to occur more frequently (86). This section examines the hypothesis that waves stimulated by convection episodes generate reflected waves in interaction with the ITCZ air column that modify the Aleutian Low Circulation.

Waves reflected from the ITCZ in December should reach the latitude of the Aleutian Low Circulation in February. Fig. 8, *Upper* shows the regressed 300-mb stream function for P1 February and P2 February. The P1 stream-function map has quasi-periodic zonal structure, whereas the P2 stream-function map has three Pacific-wide zonally aligned cells. The P2 February parity sequence is the reverse of the P2 December sequence (Fig. 4), negative–positive–negative north to south, consistent with an Arctic-origin wave train reflected in interaction with the ITCZ air column. The zonal extent of the P2 teleconnection cells suggests that reflected waves are generated along much of the ITCZ.

Fig. 8, *Lower* shows regressed 10-m wind vectors mapped over contours of SLP for P1 February (*Left*) and P2 February (*Right*). In the tropics, both SLP and surface winds are unaffected by SSIA variability in P1, whereas the P2 regression response is an increase (decrease) of SLP in the tropical Eastern (Western) Pacific. The difference in the Northern Pacific between P1 February and P2 February is notable. Smaller SSIA in P1 leads to lower SLP across the midlatitudes and a dipolar SLP anomaly further north. In P2 February, smaller SSIA leads to a single positive SLP anomaly. Its accompanying anticyclonic surface wind anomaly weakens the prevailing cyclonic Aleutian Low Circulation.

A significant response of the Aleutian Low Circulation to SSIA variability occurs only in P2 February data. The regression responses for P2 January and P2 March (not presented here) are much weaker. The off–on–off January–February–March sequence is consistent with an Arctic-origin wave train of about a month's duration that reflects from the ITCZ air column in December, propagates poleward in January, passes over the Aleutian Low Circulation in February, and enters the Arctic in March.

Remarks

Two limitations of technique prevent this paper's results from being conclusive. The first limitation stems from partitioning data into smaller subsets, risking the loss of statistical precision. For example, not separating P1 from P2 data would obscure the effects of the different teleconnection pathways linking Arctic sea ice and Pacific trade-wind variability in the two periods. The further partitioning of P1 and P2 data into monthly subsets again sacrifices precision in favor of temporal discrimination. If one accepts these risks as necessary for the problem at hand, one encounters a second limitation, circularity: To test the model, one has to assume the model. The credibility of the analysis of an individual step in the model in *Conceptual Model, Methods, and Data* depends on the credibility of the analyses of other steps in the model. The best that can be said is that at the level of precision attainable with the present methods, there is no obvious inconsistency between the results and the model used to interpret the results.

Regression has identified climatic processes that relate directly or indirectly to the variability of September Arctic sea-ice area. These include the trade-wind dipole anomaly, the Aleutian Low Circulation, the CP El Nino, and (possibly) the double ITCZ. Regression also identifies upper- troposphere telecommunication pathways connecting Arctic and tropics that could account for the regression responses at the surface. Proof that CP El Nino events triggered by Arctic origin wave trains can prompt secondary teleconnections could encourage a new view of the teleconnection network that communicates short-term climatic changes around the globe. When the El Nino feedback system is close to marginal stability, a small incoming telecommunication signal could trigger an SST response that modulates the vertical convection in the ITCZ

air column. The deep convection generated in the ITCZ air column is the main power source of the Hadley Cell overturning circulations and indirectly of global atmospheric circulation; by amplifying (or damping) teleconnection signals, the ITCZ air column becomes an active participant in the global teleconnection network.

Whether teleconnection signals are amplified or damped during their interactions with the ITCZ air column depends on the state of the Tropical Pacific Ocean, which depends on its history. Calculating rates of amplification or damping requires calculating the response of the ITCZ air column to wave-train forcing in the upper troposphere and stratosphere while exchanging energy with the subsurface ocean. Every winter provides an opportunity to make observational progress on this extraordinarily complex problem. It could prove worth the effort. ITCZ amplification of teleconnection signals could help explain how the loss of Northern Hemisphere land ice resulted in massive worldwide climate change after the Last Glacial Maximum (87).

ACKNOWLEDGMENTS. V. Ramanathan, K.K. Tung, and S.-P. Xie reviewed early drafts of this paper; they are not responsible for the errors that remain. We thank M. B. Kennel, M. J. Rees, E. Shuckburgh, and I. Zaslavski for helpful insights. We thank the reviewer who carefully pointed out where there was need for clearer presentation and our PNAS editor. C.F.K. was supported by Christ's College, Cambridge, and the University of California. E.Y. was supported by the Scripps Institution of Oceanography and the San Diego Supercomputer Center.

1. S. Manabe, R. J. Stouffer, Sensitivity of a global climate model to an increase of CO2 concentration in the atmosphere. *J. Geophys. Res. Oceans* **85**, 5529–5554 (1980).
2. J. A. Screen, I. Simmonds, The central role of diminishing sea ice in recent Arctic temperature amplification. *Nature* **464**, 1334–1337 (2010).
3. J. A. Francis, S. J. Vavrus, Evidence linking Arctic amplification to extreme weather in mid-latitudes. *Geophys. Res. Lett.* **39**, 6 (2012)
4. J. Cohen *et al*., Recent Arctic amplification and extreme mid-latitude weather. *Nat. Geosci.* **7**, 627–637 (2014).
5. Arctic Climate Impact Assessment, *Impacts of a Warming Arctic-Arctic Climate Impact Assessment, by Arctic Climate Impact Assessment* (Cambridge University Press, Cambridge, UK, 2004).
6. Arctic Monitoring and Assessment Program, *Snow, Water, Ice and Permafrost in the Arctic (SWIPA): Climate Change and the Cryosphere* (Arctic Monitoring and Assessment Program, Oslo, Norway, 2011).
7. K. Pistone, I. Eisenman, V. Ramanathan, Observational determination of albedo decrease caused by vanishing Arctic sea ice. *Proc. Natl. Acad. Sci. U.S.A.* **111**, 3322–3326 (2014).
8. R. Zhang, H. Wang, Q. Fu, P. J. Rasch, X. Wang, Unraveling driving forces explaining significant reduction in satellite-inferred Arctic surface albedo since the 1980s. *Proc. Natl. Acad. Sci. U.S.A.* **116**, 23947–23953 (2019).
9. F. Pithan, T. Mauritsen, Arctic amplification dominated by temperature feedbacks in contemporary climate models. *Nat. Geosci.* **7**, 181–184 (2014).
10. M. O. Jeffries, J. E. Overland, D. K. Perovich, The Arctic shifts to a new normal. *Phys. Today* **66**, 35–40 (2013).
11. K. E. Trenberth, J. T. Fasullo, An apparent hiatus in global warming? *Earths Futur.* **1**, 19–32 (2013).
12. C. F. Kennel, "Hiatus" in global warming: Paradox and complexity in climate science. *Proc. Am. Philos. Soc.* **159**, 367 (2015).
13. D. G. Victor, C. F. Kennel, Climate policy: Ditch the 2 °C warming goal. *Nature* **514**, 30–31 (2014).
14. M. A. Balmaseda, K. E. Trenberth, E. Källén, Distinctive climate signals in reanalysis of global ocean heat content. *Geophys. Res. Lett.* **40**, 1754–1759 (2013).
15. G. A. Meehl, A. Hu, J. M. Arblaster, J. Fasullo, K. E. Trenberth, Externally forced and internally generated decadal climate variability associated with the Interdecadal Pacific Oscillation. *J. Clim.* **26**, 7298–7310 (2013).
16. M. H. England *et al*., Recent intensification of wind-driven circulation in the Pacific and the ongoing warming hiatus. *Nat. Clim. Chang.* **4**, 222–227 (2014).
17. Y. Kosaka, S.-P. Xie, Recent global-warming hiatus tied to equatorial Pacific surface cooling. *Nature* **501**, 403–407 (2013).
18. M. Watanabe *et al*., Contribution of natural decadal variability to global warming acceleration and hiatus. *Nat. Clim. Change* **4**, 893–897 (2014).
19. X. Chen, K.-K. Tung, Climate. Varying planetary heat sink led to global-warming slowdown and acceleration. *Science* **345**, 897–903 (2014).
20. K. Ashok, T. Yamagata, Climate change: The El Niño with a difference. *Nature* **461**, 481–484 (2009).
21. S.-R. Yeo, K.-Y. Kim, Decadal changes in the southern hemisphere sea surface temperature in association with El Nino-Southern Oscillation and Southern Annular Mode. *Clim. Dyn.* **45**, 3227–3242 (2015).
22. T. Lee, M. J. McPhaden, Increasing intensity of El Niño in the central-equatorial Pacific. *Geophys. Res. Lett.* **37**, L14603 (2010).
23. H.-Y. Kao, J.-Y. Yu, Contrasting Eastern-Pacific and Central-Pacific types of ENSO. *J. Clim.* **22**, 615–632 (2009).
24. C. Fu, H. Diaz, J. Fletcher, Characteristics of the response of sea surface temperature in the central Pacific associated with warm episodes of the Southern Oscillation. *Mon. Weather Rev.* **114**, 1716–1739 (1986).
25. K. E. Trenberth, D. P. Stepaniak, Indices of El Niño evolution. *J. Clim.* **14**, 1697–1701 (2001).
26. S. W. Yeh *et al*., El Niño in a changing climate. *Nature* **461**, 511–514 (2009).
27. M. B. Freund *et al*., Higher frequency of Central Pacific El Niño events in recent decades relative to past centuries. *Nat. Geosci.* **12**, 450–455 (2019).
28. M. Feng *et al*., Decadal increase in Ningaloo Niño since the late 1990s. *Geophys. Res. Lett.* **42**, 104–112 (2015).
29. D. Coumou, S. Rahmstorf, A decade of weather extremes. *Nat. Clim. Change* **2**, 491–496 (2012).
30. Intergovernmental Panel on Climate Change, *Managing the Risks of Extreme Events and Disasters to Advance Climate Change Adaptation*, C. B. Field *et al*., Eds. (Cambridge University Press, Cambridge, UK, 2012), pp. 1–19.
31. J. Liu, J. A. Curry, H. Wang, M. Song, R. M. Horton, Impact of declining Arctic sea ice on winter snowfall. *Proc. Natl. Acad. Sci. U.S.A.* **109**, 4074–4079 (2012).
32. C. Hong *et al*., Roles of European blocking and tropical–extratropical interaction in the 2010 Pakistan flooding. *Geophys. Res. Lett.* **38**, L13806 (2011).
33. S. J. Vavrus, The influence of Arctic amplification on mid-latitude weather and climate. *Curr. Clim. Change Rep.* **4**, 238–249 (2018).
34. J. A. Screen *et al*., Consistency and discrepancy in the atmospheric response to Arctic sea-ice loss across climate models. *Nat. Geosci.* **11**, 155–163 (2018).
35. R. Blackport, J. A. Screen, K. van der Wiel, R. Bintanja, Minimal influence of reduced Arctic sea ice on coincident cold winters in mid-latitudes. *Nat. Clim. Chang.* **9**, 697–704 (2019).
36. D. Budikova, T. W. Ford, T. J. Ballinger, United States heat wave frequency and Arctic Ocean marginal sea ice variability. *J. Geophys. Res. D Atmos.* **124**, 6247–6264 (2019).
37. P. Zhang *et al*., A stratospheric pathway linking a colder Siberia to Barents-Kara Sea sea ice loss. *Sci. Adv.* **4**, eaat6025 (2018).
38. J. C. Fyfe *et al*., Making sense of the early-2000s warming slowdown. *Nat. Clim. Chang.* **6**, 224–228 (2016).
39. J. C. Stroeve *et al*., Trends in Arctic sea ice extent from CMIP5, CMIP3 and observations. *Geophys. Res. Lett.* **39**, L06801 (2012).
40. T. Koenigk, A. Devasthale, K. G. Karlsson, Arctic sea ice albedo in CMIP5 models. *Atmos. Chem. Phys.* **14**, 1987–1998 (2014).
41. D. Olonscheck, T. Mauritsen, D. Notz, Arctic sea-ice variability is primarily driven by atmospheric temperature fluctuations. *Nat. Geosci.* **12**, 430–434 (2019).
42. M. L. Kapsch, N. Skific, R. G. Graversen, M. Tjernström, J. A. Francis, Summers with low Arctic sea ice linked to persistence of spring atmospheric circulation patterns. *Clim. Dyn.* **52**, 2497–2512 (2019).
43. I. Cvijanovic *et al*., Future loss of Arctic sea-ice cover could drive a substantial decrease in California's rainfall. *Nat. Commun.* **8**, 1947 (2017).
44. S. Matsumura, Y. Kosaka, Arctic-Eurasian climate linkage induced by tropical ocean variability. *Nat. Commun.* **10**, 3441 (2019).
45. E. Kalnay *et al*., The NCEP/NCAR 40-year reanalysis project. *Bull. Am. Meteorol. Soc.* **77**, 437–471 (1996).
46. R. Kistler *et al*., The NCEP–NCAR 50-year reanalysis: Monthly means CD-ROM and documentation. *Bull. Am. Meteorol. Soc.* **82**, 247–267 (2001).
47. D. P. Dee *et al*., The ERA-Interim reanalysis: Configuration and performance of the data assimilation system. *Q. J. R. Meteorol. Soc.* **137**, 553–597 (2011).
48. E. Jakobson *et al*., Validation of atmospheric reanalyses over the central Arctic Ocean. *Geophys. Res. Lett.* **39**, L10802 (2012).
49. R. Lindsay *et al*., Evaluation of seven different atmospheric reanalysis products in the Arctic. *J. Clim.* **27**, 2588–2606 (2014).
50. W. N. Meier *et al*., NOAA/NSIDC Climate Data Record of Passive Microwave Sea Ice Concentration, Version 3 (NSIDC, Boulder, CO, 2017).
51. G. Peng, W. N. Meier, D. Scott, M. Savoie, A long-term and reproducible passive microwave sea ice concentration data record for climate studies and monitoring. *Earth Syst. Sci. Data* **5**, 311–318 (2013).
52. D. W. Behringer, Y. Xue, "Evaluation of the global ocean data assimilation system at NCEP: The Pacific Ocean" in *Proceedings. Eighth Symposium on Integrated Observing and Assimilation Systems for Atmosphere, Oceans, and Land Surface, AMS 84th Annual Meeting* . https://www.esrl.noaa.gov/psd/cgi-bin/db_search/DBListFiles.pl?did=98&tid=72048&vid=1916. Accessed 15 March 2019.
53. E. Hovmöller, The trough-and-ridge diagram. *Tellus* **1**, 62–66 (1949).
54. N. E. Graham, T. P. Barnett, Sea surface temperature, surface wind divergence, and convection over tropical oceans. *Science* **238**, 657–659 (1987).
55. N. C. Johnson, S. P. Xie, Changes in the sea surface temperature threshold for tropical convection. *Nat. Geosci.* **3**, 842–845 (2010).
56. T. Qu, Y. T. Song, C. Maes, Sea surface salinity and barrier layer variability in the equatorial Pacific as seen from Aquarius and Argo. *J. Geophys. Res. Oceans* **119**, 15–29 (2014).
57. T. Qu, J.-Y. Yu, ENSO indices from sea surface salinity observed by Aquarius and Argo. *J. Oceanogr.* **70**, 367–375 (2014).
58. K. E. Trenberth, The definition of El Nino. *Bull. Am. Meteorol. Soc.* **78**, 2771–2777 (1997).

59. J. Bjerknes, Atmospheric teleconnections from the equatorial Pacific. *Mon. Weather Rev.* **97**, 163–172 (1969).
60. S. E. Zebiak, M. A. Cane, A model El Niño–Southern Oscillation. *Mon. Weather Rev.* **115**, 2262–2278 (1987).
61. A. V. Fedorov *et al*., The impact of westerly wind bursts and ocean initial state on the development, and diversity of El Niño events. *Clim. Dyn.* **44**, 1381–1401 (2015).
62. H. Bi *et al*., Contributions of advection and melting processes to the decline in sea ice in the Pacific sector of the Arctic Ocean. *Cryosphere* **13**, 1423–1439 (2019).
63. R. Jaiser *et al*., Impact of sea ice cover changes on the Northern Hemisphere atmospheric winter circulation. *Tellus A Dyn. Meteorol. Oceanogr.* **64**, 11595 (2012).
64. J. E. Kay, A. Gettelman, Cloud influence on and response to seasonal Arctic sea ice loss. *J. Geophys. Res. D Atmos.* **114**, D18204 (2009).
65. H. Wernli, L. Papritz, Role of polar anticyclones and mid-latitude cyclones for Arctic summertime sea-ice melting. *Nat. Geosci.* **11**, 108 (2018).
66. J. A. Francis, S. J. Vavrus, Evidence for a wavier jet stream in response to rapid Arctic warming. *Environ. Res. Lett.* **10**, 014005 (2015).
67. D. Coumou, V. Petoukhov, S. Rahmstorf, S. Petri, H. J. Schellnhuber, Quasi-resonant circulation regimes and hemispheric synchronization of extreme weather in boreal summer. *Proc. Natl. Acad. Sci. U.S.A.* **111**, 12331–12336 (2014).
68. V. Limpasuvan, D. L. Hartmann, Wave-maintained annular modes of climate variability. *J. Clim.* **13**, 4414–4429 (2000).
69. C. Deser, R. A. Tomas, S. Peng, The transient atmospheric circulation response to north Atlantic SST and sea ice anomalies. *J. Clim.* **20**, 4751–4767 (2007).
70. J. A. Francis, W. Chan, D. J. Leathers, J. R. Miller, D. E. Veron, Winter Northern Hemisphere weather patterns remember summer Arctic sea-ice extent. *Geophys. Res. Lett.* **36**, L07503 (2009).
71. J. A. Francis, N. Skific, S. J. Vavrus, North American weather regimes are becoming more persistent: Is Arctic amplification a factor? *Geophys. Res. Lett.* **45**, 11–414 (2018).
72. J. M. Wallace, I. M. Held, D. W. Thompson, K. E. Trenberth, J. E. Walsh, Global warming and winter weather. *Science* **343**, 729–730 (2014).
73. B. J. Hoskins, The geostrophic momentum approximation and the semi-geostrophic equations. *J. Atmos. Sci.* **32**, 233–242 (1975).
74. J. C. Stroeve *et al*., Changes in Arctic melt season and implications for sea ice loss. *Geophys. Res. Lett.* **41**, 1216–1225 (2014).
75. K. R. Wodzicki, A. D. Rapp, Long-term characterization of the Pacific ITCZ using TRMM, GPCP, and ERA-Interim. *J. Geophys. Res. D Atmos.* **121**, 3153–3170 (2016).
76. L. Yu, S. Zhong, M. Zhou, D. H. Lenschow, B. Sun, Revisiting the linkages between the variability of atmospheric circulations and Arctic melt-season sea ice cover at multiple time scales. *J. Clim.* **32**, 1461–1482 (2019).
77. D. S. Luther, D. E. Harrison, R. A. Knox, Zonal winds in the central equatorial Pacific and El Nino. *Science* **222**, 327–330 (1983).
78. R. A. Kerr, Atmospheric science: Does a globe-girdling disturbance jigger El Nino? *Science* **285**, 322–323 (1999).
79. M. J. McPhaden, Evolution of the 2002/03 El Nino. *Bull. Am. Meteorol. Soc.* **85**, 677–695 (2004).
80. D. Chen *et al*., Strong influence of westerly wind bursts on El Niño diversity. *Nat. Geosci.* **8**, 339 (2015).
81. T. Lian, D. Chen, Y. Tang, Q. Wu, Effects of westerly wind bursts on El Niño: A new perspective. *Geophys. Res. Lett.* **41**, 3522–3527 (2014).
82. J. Qi *et al*., Salinity variability in the tropical Pacific during the Central-Pacific and Eastern-Pacific El Niño events. *J. Mar. Syst.* **199**, 103225 (2019).
83. J.-S. Kug, F.-F. Jin, S.-I. An, Two types of El Niño events: Cold tongue El Niño and warm pool El Niño. *J. Clim.* **22**, 1499–1515 (2009).
84. S. P. Xie *et al*., Eastern Pacific ITCZ dipole and ENSO diversity. *J. Clim.* **31**, 4449–4462 (2018).
85. J. E. Overland, J. M. Adams, N. A. Bond, Decadal variability of the Aleutian low and its relation to high-latitude circulation. *J. Clim.* **12**, 1542–1548 (1999).
86. S. W. Yeh, X. Wang, C. Wang, B. Dewitte, On the relationship between the North Pacific climate variability and the central Pacific El Niño. *J. Clim.* **28**, 663–677 (2015).
87. T. R. Jones *et al*., Southern Hemisphere climate variability forced by Northern Hemisphere ice-sheet topography. *Nature* **554**, 351–355 (2018).